Coastal Engineering 83 (2014) 36–48

Contents lists available at ScienceDirect

Coastal Engineering

journal homepage: www.elsevier.com/locate/coastaleng

Non-hydrostatic modeling of surf zone wave dynamics

Pieter Smit [a,*], Tim Janssen [b], Leo Holthuijsen [a], Jane Smith [c]

[a] Environmental Fluid Mechanics Section, Faculty of Civil Engineering and Geosciences, Delft University of Technology, P.O. Box 5048, 2600 GA Delft, The Netherlands
[b] Theiss Research, 30 Portola Ave, El Granada, CA 94018, USA
[c] U.S. Army Engineer Research and Development Center, 3909 Halls Ferry Road, Vicksburg, MS 39180-6199, USA

ARTICLE INFO

Article history:
Received 11 July 2013
Received in revised form 20 September 2013
Accepted 23 September 2013
Available online 22 October 2013

Keywords:
Nonlinear
Wave statistics
Non-hydrostatic
Wave breaking
Wave model
SWASH

ABSTRACT

Non-hydrostatic models such as Surface WAves till SHore (SWASH) resolve many of the relevant physics in coastal wave propagation such as dispersion, shoaling, refraction, dissipation and nonlinearity. However, for efficiency, they assume a single-valued surface and therefore do not resolve some aspects of breaking waves such as wave overturning, turbulence generation, and air entrainment. To study the ability of such models to represent nonlinear wave dynamics and statistics in a dissipative surf zone, we compare simulations with SWASH to flume observations of random, unidirectional waves, incident on a 1:30 planar beach. The experimental data includes a wide variation in the incident wave fields, so that model performance can be studied over a large range of wave conditions. Our results show that, without specific calibration, the model accurately predicts second-order bulk parameters such as wave height and period, the details of the spectral evolution, and higher-order statistics, such as skewness and asymmetry of the waves. Monte Carlo simulations show that the model can capture the principal features of the wave probability density function in the surf zone, and that the spectral distribution of dissipation in SWASH is proportional to the frequency squared, which is consistent with observations reported by earlier studies. These results show that relatively efficient non-hydrostatic models such as SWASH can be successfully used to parametrize surf zone wave processes.

1. Introduction

In the nearshore region and surf zone, ocean waves undergo a dramatic transformation mostly due to nonlinear wave–wave interactions and breaker dissipation. These dynamics play a central role in nearshore circulation and transport processes, e.g. by controlling wave setup (e.g. Longuet-Higgins and Stewart, 1964), driving nearshore currents (e.g. Longuet-Higgins, 1970; Longuet-Higgins and Stewart, 1964; MacMahan et al., 2006; Svendsen, 1984), and causing morphodynamic evolution (e.g. Hoefel and Elgar, 2003). Understanding these processes and the development of predictive models is important for both scientific research and engineering in the coastal zone. Since most coastal and coastline processes take place on much longer scales than that of the individual waves, predictive models are generally used to estimate wave statistics (e.g. significant wave height, mean period) and variations therein. However, modeling wave statistics in the nearshore is complicated both by the strong influence of nonlinear processes and an incomplete understanding of dissipation of wave energy in shoaling and breaking waves.

Stochastic (or phase-averaged) wave models for coastal applications are usually based on some form of energy (or action) balance equation (e.g. Komen et al., 1994; The WAMDI Group, 1988; Wise Group, 2007), which assumes that the wave field is (and remains) quasi-homogeneous and near-Gaussian. However, due to nonlinearity, surf zone wave statistics are generally strongly non-Gaussian, and apart from variance, higher cumulants (e.g. skewness and kurtosis) are required to completely describe the wave statistics. This poses high demands on the model representation of the nonlinear and non-conservative dynamics. In particular, for statistical models, the representation of nonlinearity invariably requires some form of closure approximation and involves evolution equations for higher-order correlations, both of which generally render the model considerably more complicated and computationally intensive (e.g. Herbers and Burton, 1997; Herbers et al., 2003; Janssen, 2006; Smit and Janssen, 2013).

Deterministic (and phase-resolving) wave models can generally incorporate nonlinearity more easily, and naturally include full coupling to the wave-induced nearshore circulations. However, although a model based on the Reynolds-averaged Navier–Stokes (RANS) equations can model surface wave dynamics in great detail, and resolve very small scales of motion (e.g. Torres-Freyermuth et al., 2007), the computational cost can become prohibitive, even for small-scale applications. For wave modeling of most coastal-scale applications, and in particular for coastal engineering, more approximate but efficient models, such as so-called non-hydrostatic models or models based on a Boussinesq approximation are generally more useable. Boussinesq-type wave models have evolved from weakly nonlinear and weakly dispersive models (see Peregrine, 1967), to nearly fully dispersive and highly nonlinear models (e.g. Madsen et al., 2002; Nwogu, 1993; Wei et al., 1995), at the expense however, of much increased complexity of the underlying model

* Corresponding author.
E-mail address: p.b.smit@tudelft.nl (P. Smit).

0378-3839/$ – see front matter © 2013 Elsevier B.V. All rights reserved.
http://dx.doi.org/10.1016/j.coastaleng.2013.09.005

equations and numerical implementations. In contrast, non-hydrostatic models are essentially numerical implementations of the basic conservation equations for mass and momentum (e.g. Ma et al., 2012; Stelling and Zijlema, 2003; Yamazaki et al., 2009), which can be directly used for wave propagation problems if sufficient spatial resolution, in particular in the vertical, is provided. As a consequence, such models are relatively simple, and grid resolution can be readily adapted to a particular application and allow propagation of waves from deep to shallow water.

However, such non-hydrostatic models (and Boussinesq models for that matter), do not model all aspects of surf-zone waves. In particular, for the sake of efficiency, these models assume a single-valued representation of the free surface in the horizontal plane, which implies that processes such as overturning, air entrainment, and wave-generated turbulence are not resolved. Instead, integral properties of breaking waves (including energy dissipation rate) are estimated by treating the breaking wave as a discontinuity in the flow variables (free surface, velocities) and maintaining momentum (and mass) conservation across the discontinuity (Smit et al., 2013). Although this gives good results for the second-order bulk statistics (such as the significant wave height), it is not clear whether such an integral approach, where some of the details of breaking waves are treated as sub-grid processes, can actually resolve the nonlinear and dissipative processes in the surf zone, and thus predict the details of the spectral evolution and nonlinear statistics there.

In the present work we set out to study these issues by comparing simulations with the non-hydrostatic model Surface WAves till SHore (SWASH, Zijlema et al., 2011) to flume observations of random waves over a 1:30 planar beach (see Smith (2004)). The motivation behind this work is to assess whether an efficient non-hydrostatic model such as SWASH can be a viable tool to study surf zone dynamics and accurately capture the statistics of strongly nonlinear and breaking waves.

In Section 2 we present the model equations, numerical approximations, and breaker modeling in SWASH. The laboratory experiments and specific model settings are described in Section 3 and we present our results (model-data comparison) in Section 4. We discuss and sum up our principal findings and their implications in Sections 5 and 6.

2. Model description

The non-hydrostatic model SWASH (Zijlema et al., 2011), is an implementation of the Reynolds-averaged Navier–Stokes equations for an incompressible, constant-density fluid with a free surface. In the present work we use this model to study one-dimensional wave propagation in a flume. In Cartesian coordinates, with x and z the horizontal and vertical coordinate respectively, and with z measured up from the still-water level z_0, the governing equations can be written as

$$\frac{\partial u}{\partial t}+\frac{\partial uu}{\partial x}+\frac{\partial wu}{\partial z}+\frac{\partial wu}{\partial z}=-\frac{1}{\rho}\frac{\partial (p_h+p_{nh})}{\partial x}+\frac{\partial \tau_{xz}}{\partial z}+\frac{\partial \tau_{xx}}{\partial x}, \tag{1}$$

$$\frac{\partial w}{\partial t}+\frac{\partial uw}{\partial x}+\frac{\partial ww}{\partial z}=-\frac{1}{\rho}\frac{\partial p_{nh}}{\partial z}+\frac{\partial \tau_{zz}}{\partial z}+\frac{\partial \tau_{zx}}{\partial x}, \tag{2}$$

$$\frac{\partial u}{\partial x}+\frac{\partial w}{\partial z}=0, \tag{3}$$

where t is time, $u(x,z,t)$ and $w(x,z,t)$ are the horizontal and vertical velocities, respectively, and ρ is the (constant) density. Further, the hydrostatic pressure $p_h=\rho g(\zeta - z)$ (with g being gravitational acceleration) and p_{nh} represents the non-hydrostatic pressure contribution. The turbulent stresses $\tau_{\alpha\beta}$ are obtained from a turbulent viscosity approximation (e.g. $\tau_{xz}=\nu\partial_z u$, with ν the kinematic eddy-viscocity) using a standard $k-\varepsilon$ model closure approximation (Launder and Spalding, 1974). The water column is vertically restricted by the (time-varying) free-surface $z=\zeta(x,t)$ and immobile bottom $z=-d(x)$. Here d is the still water depth and the location of the free surface ζ is found from continuity, expressed as

$$\frac{\partial \zeta}{\partial t}+\frac{\partial}{\partial x}\int_{-d}^{\zeta} u\,dz=0. \tag{4}$$

Eqs. (1)–(4) are solved for constant pressure at the free-surface (i.e. $p=0$), while accounting for the kinematic free-surface and bottom boundary conditions,

$$w=\frac{\partial \zeta}{\partial t}+u\frac{\partial \zeta}{\partial x} \quad (z=\zeta) \quad \text{and} \quad w=-u\frac{\partial d}{\partial x} \quad (z=-d). \tag{5}$$

At the up-wave boundary, waves are generated by prescribing the horizontal velocity $u(z,t)$ at that location, whereas opposite of the wavemaker the boundary is formed by the moving shoreline.

Since the objective is to study surf zone wave dynamics, we need to include motions in the infragravity band, which are generated in the shoaling process and released during breaking. These low-frequency components are much longer than the primary waves and much more strongly affected by bottom friction. To incorporate this, we include a bottom stress at the bottom boundary assuming a logarithmic velocity profile (Launder and Spalding, 1974) and a typical roughness height d_r.

2.1. Numerical approximations

For non-breaking waves these equations describe nonlinear shoaling, and thus include the energy transfers across different length scales in the wave spectrum due to triad and higher-order nonlinearities. The accuracy with which these processes are represented in numerical models such as SWASH, depends on the numerical methods used to approximate the governing equations, and the spatial (horizontal and vertical) and temporal resolutions used in the simulation. Moreover, when extending such models to the surf zone, careful attention must be paid to the conservation properties (in particular of momentum) of the numerical method (see Zijlema et al. (2011) for a more general discussion of the numerical methods used in SWASH).

To accurately resolve wave motion in a phase-resolving model, the horizontal resolution Δx must be a fraction of the shortest wave length L that needs to be resolved, i.e. $L/\Delta x = O(10)$. Similarly, the timestep Δt is usually a fraction of the shortest wave period T, i.e. $T/\Delta t = O(10)$. To allow for accurate, undamped propagation over long distances, SWASH uses a staggered horizontal grid combined with a second-order (in space and time), explicit, finite-difference method that is neutrally stable (no numerical damping) for small amplitude (linear theory) waves. The vertical resolution, and numerical approximations of the vertical pressure gradient, determines how well the model approximates the linear dispersion relation for surface gravity waves $\omega(k)=\sqrt{gk\ \tanh(kd)}$, which strongly affects propagation and dispersive characteristics of the wave field.

Non-hydrostatic models often make use of a boundary-fitted vertical grid that divides the instantaneous water depth $h=(\zeta+d)$ in a constant number of layers N, with variable vertical mesh-size $\Delta z = h/N$. The required number of layers N then generally depends on the deepest parts of the domain, and increases with the vertical variability of the wave-induced velocity profile, for free-surface waves represented by the relative depth kd. Hence, in shallow water ($kd \ll 1$), a coarse resolution generally suffices, whereas in deep water ($kd \gg 1$) a vertical resolution similar to the horizontal resolution is required, $\Delta z/\Delta x = O(1)$ (at least near the surface). Traditionally, this has severely limited the application of these models to wave propagation, as the number of layers required to accurately capture dispersion (say a relative error smaller than 1%) at high kd ($O(10)$) can become very large ($N > 20$), resulting in excessive computational times. These constraints are significantly relaxed in SWASH due to the use of an edge-based vertical grid combined

with a compact numerical scheme for the approximation of the vertical pressure-gradient (i.e., the Keller-box scheme; see Lam and Simpson, 1976). Hence, for $N = 6$, the maximum relative error of the numerical dispersion relation ω_n, compared with ω (or alternatively the wave celerity), remains below 0.1% for $kd < 40$ (see Appendix A). This numerical efficiency is important in the surf zone where very short waves exchange energy through nonlinear interactions, thus potentially imposing high demands on both horizontal and vertical resolutions.

2.2. Wave breaking approximations

Since SWASH assumes the free surface to be a single-valued function $\zeta(x,t)$, it cannot model processes such as overturning, air-entrainment, and the production of wave-induced turbulence after the wave form becomes unstable and breaking is initiated. However, if we are not principally interested in the details of these fine-scale processes associated with breaking waves, this approach can be very useful (and efficient) to capture the larger-scale wave and current dynamics in the surf zone (e.g. Ma et al., 2012; Smit et al., 2013).

In a non-hydrostatic model like SWASH, a breaking wave develops into a discontinuity (or hydraulic jump), which is similar to that predicted by the (non-dispersive) shallow-water equations. If momentum conservation is maintained across the discontinuity by employing shock-capturing numerical methods (in SWASH this is done using the method by Stelling and Duinmeijer, 2003) then, in analogy to hydraulic jump dynamics, energy is dissipated at a rate proportional to the cube of the bore height. In this way the entire turbulent front is essentially reduced to a sub-grid phenomenon.

However, when waves approach breaking, wave steepening introduces strong vertical gradients in the flow variables, which requires a very high vertical resolution locally to accurately capture the bore dynamics using shock-capturing numerics. If the resolution is insufficient, velocities are generally underestimated, and the initiation of breaking is delayed (Smit et al., 2013). We avoid using a fine vertical resolution by using a hydrostatic front approximation (HFA), inspired by similar developments in Boussinesq models (e.g. Tissier et al., 2012; Tonelli and Petti, 2012), and described in detail in Smit et al. (2013). The HFA method implemented here considers the (non-dimensional) rate of change of the free surface elevation, $\zeta_t' = \partial_t \zeta / \sqrt{gh}$ and forces the pressure at the wave front to be hydrostatic, i.e. $p_{nh} = 0$, once this exceeds a certain threshold (i.e. $\zeta_t' > \alpha$). Effectively, near the bore front, the model reduces to the nonlinear shallow-water equations, causing the front to assume a characteristic sawtooth-like shape, and dissipate wave energy at a rate consistent with that of a hydraulic jump. Once breaking is initiated, the breaking threshold α is reduced to β (with $\beta < \alpha$) in neighboring points to allow the breaker to more easily persist and produce more realistic breaker dynamics.

The threshold value, α, at which the HFA is initiated, depends on the wave dynamics leading up to breaking, and thus depends on the number of layers used in the model. For two layers, Smit et al. (2013) found $\alpha = 0.6$ by estimating the maximum value of ζ_t' at the observed breaking point in the experiments of Ting and Kirby (1994). Recalibration for 6 layers (as will be used here) using the same analysis method and data set as in Ting and Kirby (1994), resulted in $\alpha = 1$. This value produces similar model-data agreement for the Ting data set with the six-layer model (not shown) as found in Smit et al. (2013) for a two-layer model. The persistence parameter β was found much less sensitive to the number of layers used, and is therefore set to the value of $\beta = 0.3$ (suggested by Smit et al., 2013).

Lastly, to prevent generation of high-frequency noise in the wave profile due to the discrete activation of the HFA, some additional horizontal viscosity is introduced, of the form

$$\nu = L_{\mathrm{mix}}^2 \left| \frac{\partial U}{\partial x} \right|. \tag{6}$$

Here L_{mix} is a typical horizontal mixing length, set as a fraction μ of the local depth (i.e. $L_{\mathrm{mix}} = \mu h$), and U is the depth-averaged horizontal velocity. For $0.25 \leq \mu < 3$, this parameter supresses the generation of such noise, but has a marginal effect on the bulk energy dissipation. To minimize its influence, we set $\mu = 0.25$ in the present study.

3. Experiment and model setup

We compare SWASH simulations to a series of laboratory observations performed by Smith (2004) at the US Army Engineer Research and Development Center, Coastal and Hydraulics Laboratory. The experiments were performed in a 0.45 m wide, 45.7 m long and 0.9 m deep flume (see Fig. 1), with glass walls and a smooth concrete bottom. Waves are generated by a horizontally moving piston-type wave generator located at one end of the flume (at $x = 0$ m), and propagate over a horizontal section onto a 1:30 beach that starts at $x = 19.3$ m.

The surface elevation was measured at 10 locations (see Fig. 1), and sampled at 5 Hz for a duration of 550 s. Data acquisition was started after 50 s, thus allowing for spin-up time and prevent transient effects in the observations. The wave gauge closest to the wave maker, located on the horizontal section, is used as a boundary condition for the model. The other gauges are placed on the slope, from a depth of 0.3 m to 0.05 m, at intervals varying from 0.5 to 1.6 m (see Table 1).

Irregular waves were generated using either a single- or double-peaked spectrum. The individual spectral peaks are described by a parametric TMA shape (Bouws et al., 1985), and the high-frequency peak of the double-peaked spectra always contained two-thirds of the total energy (see Smith (2004)). In our analysis, to avoid ambiguity, we refer to the low-frequency peak as the primary peak, and to the high-frequency peak (if present) as the secondary peak; additional peaks that arise in the spectrum due to nonlinear interactions are referred to as (higher) harmonic peaks, or simply harmonics.

The experiments consider a range of incident wave conditions (see Table 2 for an overview) by varying the TMA peakedness parameter γ, considering single and double-peaked spectra, varying the peak period of the low frequency peak $T_p^{(1)} = 1/f_p^{(1)}$, and including two different significant wave heights H_{m0}. A total of 31 experiments, including 30 different wave conditions, were performed (case 11b was repeated once). If a secondary peak is included in the incident wave spectrum, it is generated at $f_p^{(2)} = 1$ Hz. The Iribarren number, ξ (definition in caption to Table) was below 0.5 (see Table 2), which suggests that the surf zone for the cases consisted mostly of spilling breakers (see e.g. Holthuijsen, 2007). Since the wavemaker was not equipped with either second-order control or reflection compensation, some spurious second-order wave motion was generated, and long waves radiated back from the beach were re-reflected into the flume.

The model domain extends from the first observation point at $x_1 = 6.7$ m, to 45 m. To ensure that the model accurately describes the wave characteristics over a wide frequency range of at least $0 \leq f \leq 4f_p$ (with f_p the peak frequency[1]), which includes the high-frequency tail, the horizontal resolution is set at $\Delta x = 0.01$ m. Such high resolution is needed to resolve the higher frequencies with wavelengths 0.1 to 0.4 m, and to accurately propagate these components over $O(10^2)$ wave lengths. Moreover, to correctly describe linear dispersion at high kd values (maximum value of kd at $4f_p$ is approximately 40), the vertical resolution is set to 6 layers, so that within the prescribed frequency range the relative error in wave celerity stays below 0.1%. From a nonlinear perspective, this also ensures that the resonant mismatch is well predicted for interactions below $4f_p$ (see Appendix A). Time integration was performed for a duration of 600 s with a time step of $\Delta t = 0.005$ s (so that $4f_p\,\Delta t \geq 50$ in all cases). The bottom roughness height d_r was set to a value of 4.5×10^{-4} m, which is representative

[1] Note that $f_p^{(1)}$ and $f_p^{(2)}$ specifically refer to the locations of the incident waves, whereas we will use f_p to refer to the local peak frequency. We will use the same convention for peak wave periods and wave numbers.

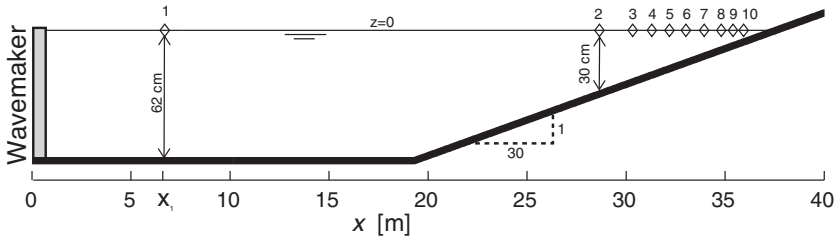

Fig. 1. Layout of the flume experimental setup by Smith (2004). The diamond markers at still-water level ($z = 0$) indicate measurement locations.

for smooth concrete (e.g. Chow, 1959). Each individual simulation (each case) takes approximately 30 min to complete on a 6-core Intel Xeon 3.2 GHz CPU desktop computer.

3.1. Wave forcing

The model is forced with the measured free-surface records at the first wave gauge, which implies that the model-data comparisons are essentially deterministic. To directly force the model using the data, we relate the time-varying, layer-averaged horizontal velocity $u_n(t)$ for each vertical layer n (with $n = 1…N$, and $n = 1$ denoting the bottom layer), required to drive the model at the up-wave boundary, to the measured free-surface elevation at that location. Therefore we consider the Fourier sum of the free-surface elevation and horizontal velocity,

$$\zeta(t) = \sum_{j=-J}^{J} \hat{\zeta}_j \exp\left[i2\pi f_j t\right], \qquad u(z,t) = \sum_{j=-J}^{J} \hat{u}_j(z) \exp\left[i2\pi f_j t\right], \tag{7}$$

where $f_j = j\Delta f$, $\Delta f = 1/T$ and $i^2 = -1$. The horizontal velocity (using linear wave theory) is found from

$$\hat{u}_j(z) = 2\pi f_j \hat{\zeta}_j \frac{\sinh\left[k_j(z+d)\right]}{\sinh\left(k_j d\right)} \tag{8}$$

where k_j is the wavenumber related to f_j by the linear dispersion relation. The layer-averaged velocity $u_n(z,t)$ is then obtained by integration over the nth layer, and subsequently dividing by the layer thickness,

$$u_n(z,t) = \frac{1}{\Delta z} \sum_{j=-J}^{J} \int_{z_{n-1}}^{z_n} \hat{u}_j(z,t) \exp\left[i2\pi f_j t\right] dz, \tag{9}$$

where $z_n = n\Delta z - d$ and $\Delta z = d/N$.

Although presumably, due to the lack of second-order control, some spurious and second-order low-frequency motion is generated at the wavemaker, most of the low-frequency energy present at the offshore gauge consists of low-frequency energy generated in the breaking process through subharmonic triad interactions, reflected off the beach, and subsequently re-reflected off the wavemaker. To model this consistently, the model is forced with the high-pass filtered observed time series (for $f > f_p{}^{(1)}/2$) at the offshore gauge (gauge 1), and the offshore boundary is set to be fully reflective (to mimic the reflecting wavemaker). In this way, the low-frequency motion is thus not forced into the model at the wavemaker, but allowed to develop in the surf zone and reflect back into the model domain (as happens in the flume).

Table 1
Instrument location (x) and still-water depth (d) during experiments (see Smith, 2004).

Gauge	1	2	3	4	5	6	7	8	9	10
x (m)	6.7	28.7	30.3	31.3	32.2	33	33.9	34.8	35.4	35.9
d (m)	0.62	0.3	0.24	0.21	0.18	0.15	0.12	0.09	0.07	0.05

4. Results

To asses overall model performance we first consider several bulk parameters. In particular, we consider significant wave height $H_{m_0} = 4\sqrt{m_0}$ and mean period $T_{m02} = \sqrt{m_2/m_0}$, where $m_n = \int f^n E(f) df$, and higher-order bulk statistics of skewness Sk and asymmetry As, which are defined as

$$\mathrm{Sk} = \frac{\left\langle \zeta^3 \right\rangle}{\left\langle \zeta^2 \right\rangle^{3/2}}, \quad \mathrm{As} = \frac{\left\langle \zeta_h^3 \right\rangle}{\left\langle \zeta^2 \right\rangle^{3/2}}. \tag{10}$$

Here ζ_h is the Hilbert transform of ζ (from which the mean contribution is subtracted) and $\langle \ldots \rangle$ denotes a time average.

The significant wave height and mean period are second-order bulk statistics which are a measure of the total amount of energy, and a measure of period, respectively. The mean period T_{m02} also provides some insight in the distribution of wave energy across frequencies. Skewness and asymmetry are third-order bulk statistics, measuring the wave asymmetry, around a horizontal and vertical plane, respectively. Positive skewness is associated with steeper, higher peaks and flatter troughs (e.g. second-order Stokes waves), and negative asymmetry is associated with the forward pitching, saw-tooth like appearance of waves in the surf zone (Elgar and Guza, 1985). Since for a Gaussian wave field both skewness and asymmetry are zero (as are all cumulants higher than the second), the comparison between observed and modeled skewness and asymmetry values measures the accuracy of

Table 2
Wave conditions considered in the experiments by Smith (2004). $T_p^{(1)}$ refer to the primary peak period, whereas $T_p^{(2)}$ refers to the period of the secondary peak (if applicable). Wave steepness is defined from the wave number spectrum $E(k)$, with k the wave number, as $\sqrt{\int k^2 E(k) dk}$. The Iribarren number ξ is defined as $\xi = tan\alpha / \sqrt{H_{m0}/L_p}$, with H_{m0} the significant wave height as listed, $tan\alpha = 1/30$ the bottom slope and $L_p = g(T_p^{(2)})^2/2\pi$ the deep-water wavelength. Listed values for $k_p^{(1)}d$ are calculated using the primary peak period and $d = 0.62$ m. All other variables are defined as in the main text. Cases considered individually in figures or discussed in the main text are marked with an asterisk.

Case	$T_p^{(1)}$	$T_p^{(2)}$	H_{m0}	γ			Wave steepness			$k_p^{(1)}d$	ξ
				(a)	(b)	(c)	(a)	(b)	(c)		
1	2.5	1.0	9.0	3.3*	20	100*	0.13	0.12	0.11	0.68	0.34
2	2.0	1.0	9.0	–	20*	–	–	0.12	–	0.88	0.27
3	1.75	1.0	9.0	3.3	20*	100	0.13	0.13	0.11	1.00	0.24
4	1.5	1.0	9.0	–	20	–	–	0.13	–	1.3	0.20
5	1.25	1.0	9.0	3.3	20	100	0.14	0.13	0.12	1.7	0.17
6	2.5	–	9.0	3.3*	20	100*	0.07	0.05	0.05	0.68	0.32
7	2.0	–	9.0	–	20*	–	–	0.04	–	0.88	0.26
8	1.75	–	9.0	3.3	20*	100	0.1	0.07	0.05	1.00	0.23
9	1.5	–	9.0	–	20	–	–	0.06	–	1.3	0.20
10	1.25	–	9.0	3.3*	20	100*	0.13	0.11	0.08	1.7	0.17
11	1.0	–	9.0	3.3*	20*	100*	0.15	0.12	0.13	2.5	0.14
12	2.5	1.0	6.0	–	20	–	–	0.08	–	0.68	0.41
13	2.0	1.0	6.0	–	20	–	–	0.08	–	0.88	0.32
14	1.75	1.0	6.0	–	20	–	–	0.08	–	1.00	0.28
15	1.5	1.0	6.0	–	20	–	–	0.09	–	1.3	0.25
16	1.25	1.0	6.0	–	20*	–	–	0.09	–	1.7	0.20

the nonlinear dynamics in the model, and – in the surf zone – the interplay between nonlinear and dissipative processes (Chen et al., 1997).

All spectral estimates (for calculations and observations) are obtained from detrended and windowed Fourier transforms of 18.3 s length segments with 50% overlap, which are subsequently ensemble averaged to yield estimates for $E(f)$ with a resolution of $\Delta f = 0.055$ Hz and approximately 110 degrees of freedom.

The spatial evolution of the significant wave height and the mean period in the surf zone is generally well captured by the model as illustrated by the eight cases shown in Fig. 2. These results are representative and similar results were found for the other cases (not shown). It can be seen that the location where intense breaking starts (abrupt decrease in wave height), and the spatial variations in mean period through the surf zone, are accurately resolved by the model. Only at gauge 8 ($x = 34.8$ m third observation point from the right), the model systematically under-predicts the observed wave heights. Variations in T_{m02} are, apart from dissipation, also strongly affected by nonlinearity. In the shoaling region, i.e. outside the surf zone proper, T_{m02} is reduced by the development of higher harmonics in the wave spectrum (to be treated below, see Fig. 4), whereas inside the surf zone short waves are rapidly dissipated and nonlinearity drives the generation of low-frequency infragravity waves, thus resulting in the observed (and modeled) increase in T_{m02}.

On the horizontal section, the waves are weakly nonlinear, with low asymmetry and skewness values, generally consistent with Stokes second-order waves. On the slope, skewness increases as the waves become more 'peaked', and asymmetry takes on larger negative values, indicative of the pitch-forward shapes developing as the wave approaches breaking (or are breaking). Near the shore, the magnitude of skewness and asymmetry generally reduces resulting in statistics that are closer to Gaussian. The variability of these third-order statistics is quite accurately reproduced by the model (see Fig. 2). For the narrow-band case, 6c, there is somewhat less good correspondence between observed and modeled surf zone wave asymmetry than for the other cases (see Fig. 2n, black line/markers). This is likely due to the hydrostatic bore approximation which generates near-vertical fronts in breaking waves, whereas in reality wave-induced turbulence would stabilize the front toward a more moderate slope of the face of the breaking wave (e.g. Madsen and Svendsen, 1983). This exaggeration of wave asymmetry by the hydrostatic bore approximation, mostly affects narrow-band waves; in wider-band wave fields (e.g. case 6a shown in panel m of Fig. 2), which we are more likely to encounter on natural beaches, the intermediate steep bores ride on a background of irregular smooth waves, which apparently smoothes the statistics, and produces model results in very close agreement with observations (see Fig. 2).

Considering all 31 cases, the comparison between observed and modeled bulk statistics shows excellent agreement (see Fig. 3), with R^2 values larger than 0.9. The agreement is best for the significant wave height and period. For the wave heights, there is however a clustering of points that lie below the main diagonal. This cluster is associated with observations made by gauge 8, which (as seen before in Fig. 3a) recorded consistently slightly higher values than model predictions for all cases and wave conditions, and which stands out relative to other (surrounding) observations (see Fig. 3a). Moreover, the fact that there are no such differences in the results for T_{m02}, the skewness or asymmetry, led us to believe that these differences are due to a slight gauge calibration inconsistency (experimental error), rather than a systematic model error.

The higher-order statistics of skewness and asymmetry are in excellent agreement, but have slightly more scatter. Skewness is generally slightly under-predicted, whereas the modeled asymmetry is slightly more negative than observed. However, these higher-order statistics strongly depend on both nonlinearity and a correct representation of wave dissipation, and the good agreement suggest that the model captures these processes very well.

4.1. Evolution of wave spectra

Apart from dissipation and linear shoaling effects, the enhancement of skewness, asymmetry, and the evolution of T_{m02} in the surf zone (see Fig. 2), indicate that redistribution of energy due to nonlinear triad

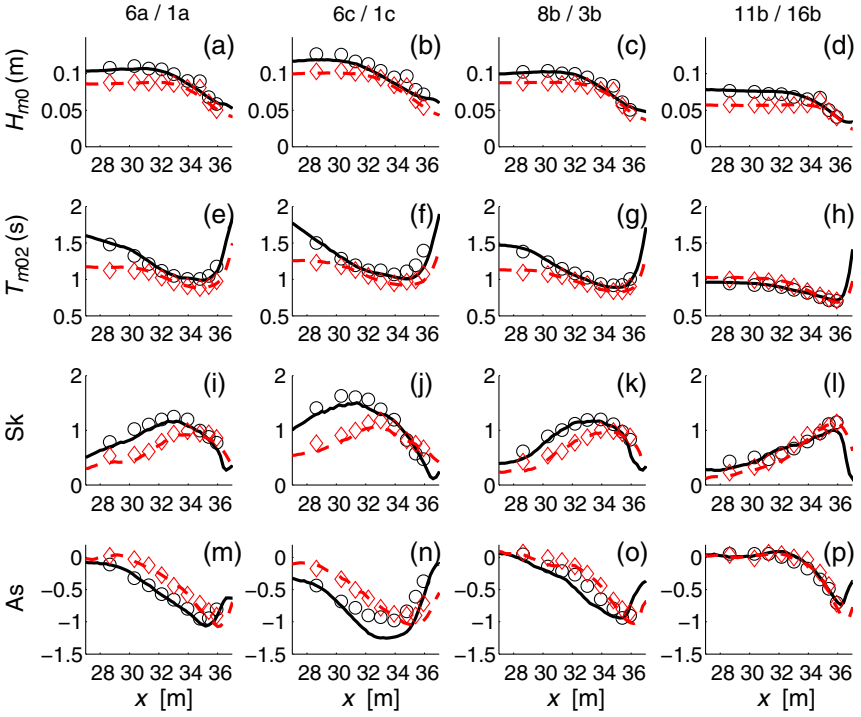

Fig. 2. Comparison between modeled (lines) and observed (symbols) values of significant wave height (panels a–d), mean period (e–h), skewness (i–l) and asymmetry (m–p). In each column a single-peaked (black solid line/circles) and double-peaked (red dashed line/diamonds) case with the same H_{m0} $T_p^{(1)}$, and γ are shown (the only difference between these cases is the single- or double-peakedness of the spectrum). Case numbers (single/double) are indicated above each column.

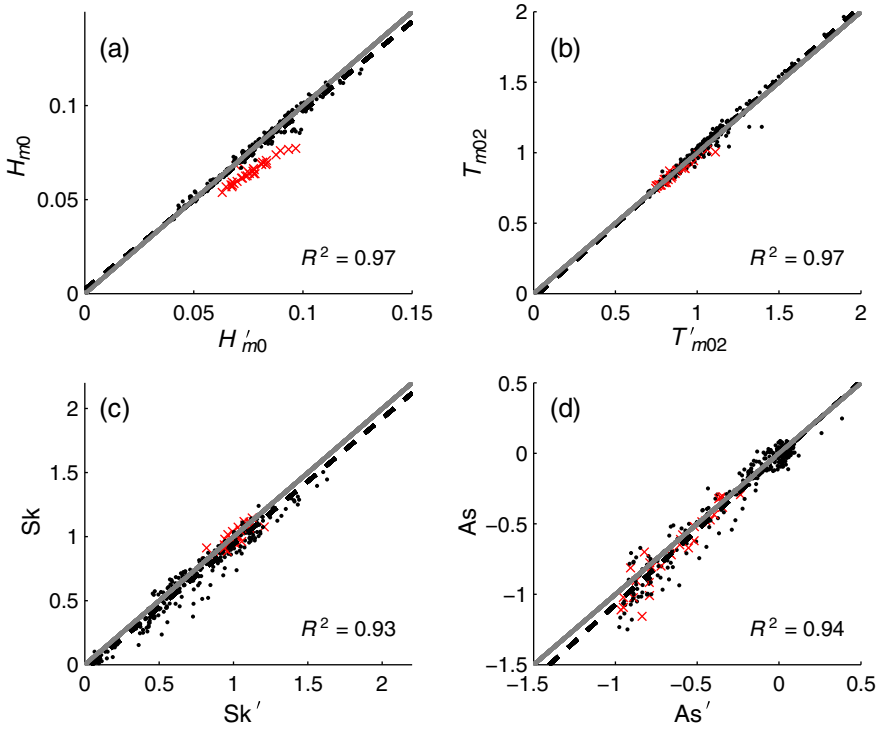

Fig. 3. Scatter plots of observed (primed variables) versus computed values for: (a) significant wave height, (b) mean period, (c) skewness and (d) asymmetry. The solid gray line indicates one-to-one correspondence, whereas the dashed line is the best fit regression line (R^2 values indicated in each panel). Red crosses correspond to values obtained from observations at gauge 8.

interactions plays an important role in the wave evolution. To investigate this in more detail we consider the evolution of observed and modeled spectra.

Harmonic amplification due to triad interactions becomes more pronounced in shallow water since the interactions approach resonance. The development of such higher harmonic contributions is most pronounced for narrow-band waves where the primary and harmonic peaks are well defined, with limited phase mixing. For instance, for case 6c ($k_p^{(1)}d = 0.68$, $\gamma = 100$) some harmonic amplification already occurs on the flat (see Fig. 4a), and at gauge 2 we can clearly distinguish – in both the model and the observations – the first three harmonics of the peak (0.4 Hz), located at 0.8, 1.2 and 1.6 Hz respectively (see Fig. 4a). In the surf zone (Fig. 4b–c), the combined effects of three-wave interactions and dissipation due to wave breaking strongly attenuate the spectral peaks, so that in the inner surf zone only the primary peak and sub-harmonics remain. Qualitatively, the picture is similar for other cases although for higher-frequency incident waves (e.g. case 11c, Fig. 4d–f) and more broad-banded wave fields (e.g. case 1a, Fig. 4j–l) the harmonic development is less pronounced.

There are several sources of long wave motion in the flume. In the shoaling process, three-wave interactions amplify bound long-wave components (here roughly defined as components with frequencies $f < 0.5\ f_p$), which are subsequently released in the breaking process (e.g. Battjes et al., 2004; Janssen et al., 2003). Most of the energy contained in these frequencies subsequently reflects at the beach and radiates back out through the surf zone as free long waves. In the field such components would continue to propagate offshore (unless refractively trapped), but in the flume they are almost completely re-reflected by the wavemaker. Although some low-frequency energy is associated with second-order bound waves, and some spurious wave motion due to the first-order wavemaker control, by far the largest contribution to the low-frequency energy is associated with these reflected and re-reflected free-wave components generated in the shoaling and breaking process by nonlinear three-wave interactions (see e.g. Battjes et al., 2004). The level of agreement between model and observations suggests that the nonlinear surf zone wave-dynamics are captured accurately. The remaining differences between model and observations could be due to errors in the estimate for bottom friction, which is one of the primary mechanisms (in addition to breaking of long waves, e.g. van Dongeren et al., 2007) by which the longer waves loose energy.

One aspect that makes the present experimental dataset (Smith, 2004) particularly interesting, is the fact that it includes several cases with double-peaked spectra. These cases show a dramatic spectral evolution across the flume. Similar to previous laboratory observations by Smith and Vincent (1992), the secondary peak, which initially contains the bulk of the energy, diminishes rapidly on the slope, whereas the low frequency peak appears to grow at its expense. This behavior, which is also largely due to triad interactions, is clearly seen in the observed spectra for the double peaked cases, both for narrow or wide-band initial spectra, as exemplified here in cases 1c and 1a, respectively (see Fig. 4, panels g–l). The model also reproduces this reduction of the secondary peak (at 1 Hz), which is initially still visible at gauge 2 (panels g/j), but has virtually disappeared at gauges 6 (panels h/k) and 10 (panels i/l).

4.2. Energy fluxes

The effects of nonlinearity and dissipation on the various spectral regions can be further illustrated by considering the spatial evolution of the linear energy flux, $F(f,x) = c_g E(f,x)$ at distinct frequencies. Since for linear and conservative wave propagation the wave energy flux is constant, changes in this flux indicate where nonlinear effects and dissipation are present. To reduce the sensitivity of the results to the details of the spectral analysis (e.g. such as the frequency resolution), we consider the normalized flux integrated over a finite frequency band Δf_n,

$$\Delta F_n(x) = \frac{\int_{\Delta f_n} F(f,x)df}{F_{\mathrm{tot}}(x_1)}, \tag{11}$$

where we normalized with the total energy flux $F_{\mathrm{tot}}(x) = \int F(f,x)df$ at the up-wave boundary (located at x_1). The frequency band Δf_n is defined

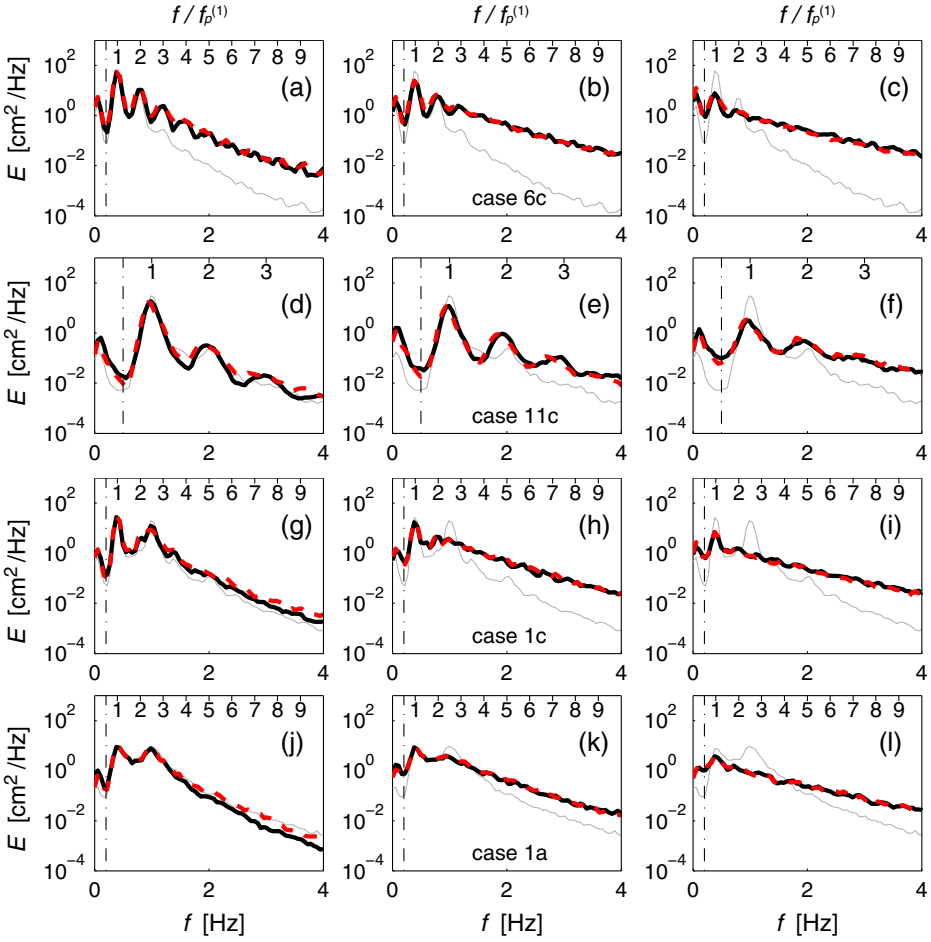

Fig. 4. Comparison between the observed (dashed red lines) and computed (solid black lines) energy density spectra for four different cases (ordered from top to bottom) at gauge 2 (left panels), gauge 6 (center panels), and gauge 10 (right panels). The lower horizontal axis indicates the absolute frequency, whereas the upper axis in each panel indicates the relative frequency $f/f_p^{(1)}$. Incident wave spectrum at the up-wave boundary is indicated by the thin gray line and the dash–dot line indicates the upper frequency ($f_p^{(1)}/2$) of the infra-gravity (ig) range.

as a narrow frequency band around the nth harmonic frequency, i.e. Δf_n is defined as the interval $0.95(n+1)f_p^{(1)} < f < 1.05(n+1)f_p^{(1)}$. In the following we consider the integrated energy flux for the primary peaks (ΔF_0), and their respective first (ΔF_1) and second harmonics (ΔF_2).

On the flat and at the start of the slope, the model shows near constant energy fluxes (see Fig. 5), indicating that there is very little dissipation or nonlinear transfers before the waves reach the slope. On the slope, the energy flux for the primary peak reduces, in part due to dissipation, and in

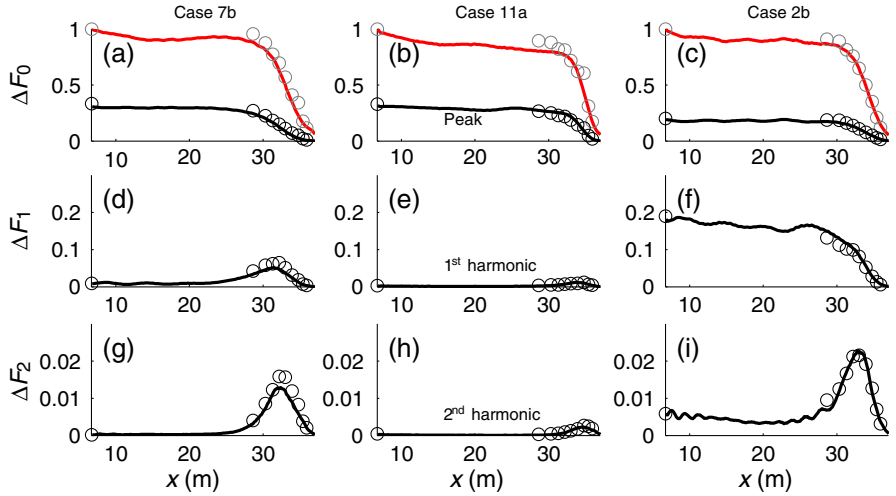

Fig. 5. Comparison between the observed (symbols) and computed (lines) energy flux ΔF_n (defined in Eq. (11)) contained in a frequency band around the peak (panels a–c), the first harmonic (panels d–f) and the second harmonic (panels g–i). Each column represents a different case (indicated on top). In the upper panels (a–c) the normalized total flux ($=F_{tot}(x)/F_{tot}(x_1)$) is included (red lines/symbols) for reference.

part due to transfers to higher and lower frequencies, consistent with the increase in energy flux at the harmonic peaks at roughly the same location.

At the start of the slope ($x = 19$ m, see Fig. 1), dissipation is still weak as the total energy flux remains constant, so that for relatively long, narrow-band waves (e.g. case 7b, with $k_p^{(1)}d = 0.88$, $\gamma = 20$) the amplification of the higher harmonics can be clearly distinguished (panels a, d, and g in Fig. 5). In case of relatively high-frequency, broad-banded waves (e.g. case 11a, with $k_p^{(1)}d = 2.5$, $\gamma = 3.3$) such amplification is less pronounced, as the waves are in relatively deeper water and three-wave interactions therefore further from resonance. Moreover, for broad-banded waves, each frequency participates in more triads, thus broadening the resulting secondary peaks and resulting in less distinct spectral features than for narrow-band waves. Further up the slope, for higher-frequency, broader-band cases, amplification generally occurs only in the very shallow part of the flume (e.g. panels b, e, and h in Fig. 5). For both broad and narrow-banded cases, once dissipation becomes dominant, the energy fluxes around the peak and its harmonics are rapidly reduced. Overall, observed and modeled evolution of the primary and harmonic energy bands is in very good agreement.

The difference between the evolution of a single and double peaked spectrum is illustrated by comparing case 7b with case 2b, which differ only in their spectral shape. The evolution of the total energy flux, and that of the primary peak is relatively similar (viz. panels a and c in Fig. 5). However, for $20 < x < 30$ no amplification occurs at the secondary peak (see Fig. 5f), despite the fact that in this case it coincides with the 1st harmonic of the primary peak (i.e. $f_p^{(2)} = 2f_p^{(1)}$. In contrast, even before the onset of strong dissipation (which occurs for $x > 30$, see Fig. 5c), the energy flux around the secondary peak is attenuated, presumably due to nonlinear transfer to other frequencies. The regions where amplification and attenuation of the energy flux around the 2nd harmonic ($3f_p^{(1)}$) occur, and the relative magnitudes of the respective fluxes, are again very similar (viz. Fig. 5g and i).

The overall performance of the model with regard to ΔF_n, including contributions up to the second harmonic, is summarized in the scatter plots in Fig. 6a–c. The absence of outliers, and the high R^2 values, confirms that the model captures the development up to and including the second harmonic very well. It should be noted that R^2 values in this case are inflated due to the large range within the data, where the highest and lowest ΔF_n can differ a factor factor 10^2; even for large relative errors, small values in the data contribute little to the total variance of the error, but significantly to the observed variance, thus somewhat inflating values of R^2.

4.3. Shape of the high-frequency tail in the surf zone

The wave spectra presented in Fig. 4 demonstrate that the strong amplification of the spectral energies in the high-frequency tail ($f > 2.5f_p$), by at least an order of magnitude when compared to the incident spectra, is reproduced by the model. Furthermore, in all cases the model relaxes the high frequency tail into a fairly featureless shape in the surf zone. The development of such an asymptotic form in shallow water has been previously observed in both field and laboratory observations, which led Smith and Vincent (2003) to propose a universal parametric tail in the surf zone. Expressed in terms of the wave number spectrum $E(k)$ (obtained form a linear transformation), their parametric tail consists of two ranges: the Toba range ($kd > 1$), and the Zakharov range ($2k_pd \le kd \le 1$, with k_p the peak wave number). For the Toba range, Smith and Vincent (2003) found that the spectrum scales as $E(k) \sim k^{-5/2}$. For the Zakharov range they found that the spectrum scales as $E(k) \sim k^{-4/3}$, similar to the tail in shallow water proposed by Zakharov (1999). As noted by Kaihatu et al. (2007), referring to these ranges as the Toba and Zakharov range is somewhat questionable for strongly nonlinear, breaking surf zone waves. Toba proposed his asymptotic form based on observations of wind-driven, deep-water waves (which obviously does not apply here), and the strongly nonlinear conditions found in the surf zone are outside the range where the theory by Zakharov (1999) can be applied. Regardless of whether the eponymous naming of these spectral ranges is entirely justified, the observations considered by Kaihatu et al. (2007) generally supported the results of Smith (2004) at the edge of the surf zone, although they also found that the spectrum has a clear $E(k) \sim k^{-2}$ asymptote in very shallow water.

Because in the present data set the Zakharov range only exists at the most shoreward location (elsewhere $2k_pd > 1$), we extended – following Kaihatu et al. (2007) – this range to $k_pd \le kd \le 1$. For each case we transformed the spectra to wavenumber space using linear theory, and determined the exponent, n, of the shape function αk^n that best fitted the data from the slope of the linear regression line between *log* $[E(k)]$ and log (k). This analysis was performed for the Zakharov and Toba ranges separately, yielding a value for n in either range at each separate gauge for all of the 31 experiments. Subsequently, at each gauge the mean value and the standard deviation were determined, yielding a mean value n_{Zak} and n_{Toba}, and standard deviation σ_{Zak} and σ_{Toba}, for the Zakharov and Toba range respectively, the results of which are shown in Fig. 7.

In very shallow water ($d < 015$ m), the mean value of n_{toba} compares well with the earlier reported values (see Fig. 7a); it tends to $-5/2$ with relatively small scatter around the mean in both the observed or computed data ($\sigma_{Toba} < 0.1$ for $0.05 < d < 0.12$ m). For increasing depth, values for n_{toba} obtained from computed spectra are at some variance with the observations ($d > 0.2$ m), with increased scatter around the mean ($\sigma_{Toba} > 0.3$), but generally larger scatter in the computed than in the observed results. This larger scatter in the spectral shape for the Toba range in the deeper parts of the flume, and also the

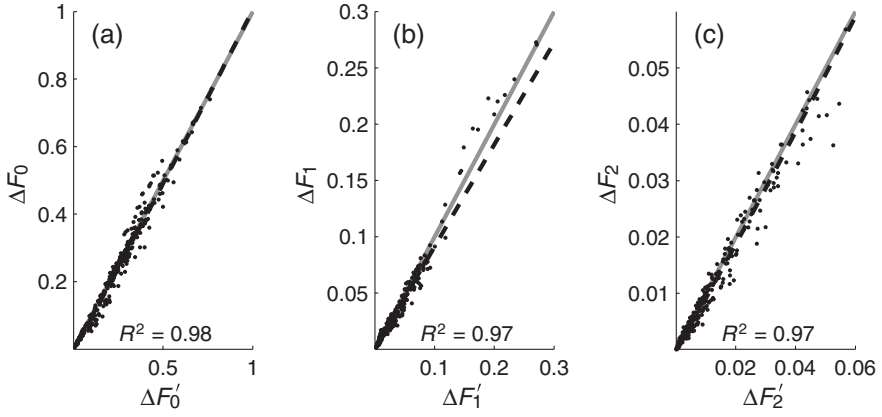

Fig. 6. Comparison between the observed $\left(\Delta F'_n\right)$ and computed (ΔF_n) normalized energy fluxes at the primary peak (left panel), and its first (middle panel) and second (right panel) harmonic. The gray line indicates one-to-one correspondence, whereas the dashed line is the best fit linear regression line (R^2 values given in panels).

lesser agreement with observations, are likely due to being in the vicinity to the wavemaker, so that the spectrum is still adjusting from the artificial wavemaker input, and has not yet developed into an equilibrium shape. A better correspondence with the observed tail most likely requires that the numerical wavemaker exactly reproduces the high-frequency tail, including possible nonlinear contributions.

For the Zakharov range, the agreement with observations, both in the mean trend and in the scatter, is excellent (Fig. 7b), with good correlation ($R^2 = 0.97$) between results obtained from observations and computations (not shown). However, although the averages in the surf zone are close to theoretical value of $n_{zak} = -4/3$ (they are -1.3 and -1.41 for observations and model, respectively), neither the model nor the observations appear to converge to this value when nearing the shoreline. In general, the scatter is quite large, but near the shoreline (between a depth of 0.05 to 0.1 m) σ_{Zak} this scatter is significantly reduced, both in the observations (from 1.3 to 0.3) and computations (from 1.3 to 0.1). As $d \to 0$ the model seems to converge to $n_{zak} = -1.9$ with $\sigma_{Zak} = 0.08$, in accordance with $E(k) \sim k^{-2}$ asymptote in very shallow water as found by Kaihatu et al. (2007).

4.4. Nonlinear energy transfer

In shallow water, the dominant nonlinear energy transfer is associated with near-resonant triad interactions, the strength of which generally depends on the coupling coefficient, energy content of the components involved in the interaction, and how close the interaction is to resonance. To compare transfer rates inferred from observations and model results therefore requires the evaluation of a nonlinear source term S_{nl} that depends on the bipectrum $B(f_1,f_2,x)$, and which has the general form (e.g. Becq-Girard et al., 1999; Herbers and Burton, 1997; Janssen, 2006)

$$S_{nl}(f) = 4\int_0^f C\left(f', f-f'\right)\mathcal{B}_{im}\left(f', f-f'\right)df' - 8\int_0^\infty C\left(f+f', -f'\right)\mathcal{B}_{im}\left(f, f'\right)df', \tag{12}$$

where C is a (real) coupling coefficient and $\mathcal{B}_{im}$ denotes the imaginary part of the bispectrum. The bispectrum captures the phase relationship between a triad of waves f_1, f_2 and $f_3 = f_1 + f_2$, and describes the third-order statistics of the wave field. For instance, skewness and asymmetry can be obtained from the real or imaginary part of the integral over the bispectrum, respectively, i.e. $\mathrm{Sk} + i\mathrm{As} = \iint \mathcal{B}(f_1,f_2)df_1df_2/m_0^{3/2}$. The source term $S_{nl}(f)$ includes all sum and difference contributions to frequency f. For second-order Stokes waves on a horizontal bottom $\mathcal{B}_{im}(f_1,f_2) = 0$, and no energy transfer occurs.

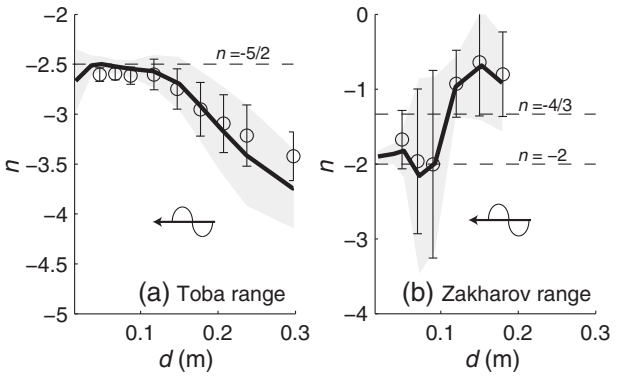

Fig. 7. The slope n of best fit line to the log of the wavenumber spectrum $E(k)$ within the Toba ($kd > 1$) and Zakharov ($k_p < kd < 1$) range. In both panels the mean n as calculated from observations (symbols) and from model results (line) is plotted as a function of depth. The region that lies within one standard deviation from the mean is indicated by bars for the observations, and as a shaded area for the model simulations. The arrow indicates that the wave direction in the figure is towards shallow water.

Since the observation points are in shallow water ($k_pd < 1$) we use Boussinesq theory (Herbers and Burton, 1997; Herbers et al., 2000) to evaluate S_{nl}, so that $C(f_1,f_2) = 2\pi(f_1 + f_2)/d$. The use of Boussinesq theory only affects the interaction kernel, which will be the same for both model results and observations (the bispectrum is estimated from observations and model results directly), so that the intercomparison is consistent. We approximate the integrals over the bispectrum using the trapezoidal rule with an upper-frequency of 6 Hz in the second term on the RHS of Eq. (12). Bispectra are obtained using the same spectral analysis of observed and computed time series as before.

Results for three representative cases, including a wide (10a), narrowband (10c), and double-peaked (3b) incident spectrum, are shown in Fig. 8. The transfer rates computed from the model simulation results are in good agreement with the values computed from the observations, with overall better correspondence in the energetic part of the spectrum ($f < 2f_p$), and slightly worse correspondence in the tail. The nonlinear interactions transfer energy from the primary peak(s) of the spectrum to the higher (and lower) frequencies. For instance, in case 10c at gauge 5 (Fig. 8c), energy is transferred from the spectrum peak ($f = 0.8$ Hz), to its first ($f = 1.6$ Hz), second ($f = 2.4$ Hz) and (presumably) higher harmonics. In the case of more broad-banded irregular waves, the great number of interactions that take place result in a more uniform shape of S_{nl} at the frequencies above the peak (e.g. Fig. 8a/c). In the inner surf zone (gauge 10), energy is mostly transferred from $0.5f_p \le f \le 2f_p$, toward higher frequencies ($f > 2f_p$), regardless of the width of the incident spectrum (viz. case 10a with case 10c in Fig. 8e/f, respectively).

In the absence of dissipation S_{nl} approximately balances with F_x, and large differences between S_{nl} and F_x are therefore indicative of dissipation. The gauge spacing (varying from 0.5 to 1.6 m) is too large to obtain estimates for F_x from the observations directly in the highly dynamic surf zone. However, such estimates can be readily obtained from the more finely spaced model results using second-order finite differences,

$$Fx(f,x) \approx \frac{F(f,x+\Delta x) - F(f,x-\Delta x)}{2\Delta x} \tag{13}$$

where Δx is the computational mesh-size. Near the peak of the spectrum (see Fig. 8 panels a–c) changes in F_x are approximately balanced by S_{nl}, suggesting that for $f < 2f_p$ the evolution of the spectrum is primarily determined by nonlinearity whereas the dissipation rates – even in the inner surf zone – remains relatively small in this spectral range (e.g. panels d–f). For $f > 2f_p$ the evolution of F_x is minimal, suggesting that dissipation and nonlinear transfers are nearly in balance. This (model) behavior shows that energy is not dissipated in the energetic range of the spectrum, but instead is transferred from the peak to the higher frequencies, where it is subsequently dissipated, consistent with observations by other researchers (e.g. Herbers et al., 2000).

5. Discussion

The results presented thus far are quasi-deterministic, in the sense that all results were derived from a single, relatively short realization using deterministic boundary conditions. The differences between model and observations can therefore be ascribed to modeling inaccuracies (we ignore measurement noise or errors, except for the possible gauge calibration issue at gauge 8) and are not due to uncertainty in statistical estimates, which would be inevitable for a finite-length time series. Since the deterministic comparison showed excellent agreement between model and data for all relevant surf zone wave processes studied here, we expand on this here to study the surf zone statistics and dissipation characteristics from Monte Carlo simulations with the model. The Monte Carlo simulations consist of 10 realizations for each case considered. Each realization is forced with randomized initial conditions (from the observed spectrum with added random phases). This extends the total number of data points N^{tot} from 12×10^4 to 1.2×10^5.

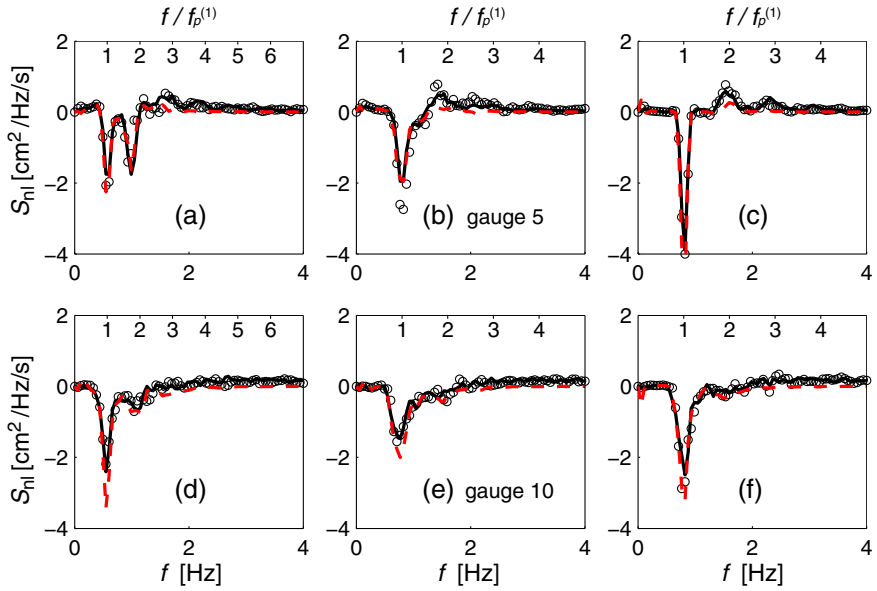

Fig. 8. The nonlinear source term S_{nl} computed at two different gauges (ordered from top to bottom) for case 3b (left panels), case 10a (middle panels), and case 10c (right panels). The source term is computed from the bispectrum obtained from the observations (markers) and computations (solid black line). In addition the linear flux gradient F_x (dashed red line) estimated from model results is included. The lower horizontal axis indicates the absolute frequency, whereas the upper axis in each panel indicates the relative frequency $f/f_p^{(1)}$.

For these 2DV simulations (1D wave propagation), the complete Monte Carlo simulation (10 realizations) takes about 300 min per case on a 6-core Intel Xeon 3.2 GHz CPU. When considering 2D wave propagation, computational times are considerably higher but feasible on larger multi-processor systems, in particular since even a more coarse vertical grid (i.e. 2 vertical layers) can still yield reliable estimates for the bulk parameters and wave spectrum up to three times the peak frequency (see e.g. Smit et al., 2013).

5.1. Free-surface statistics

The probability density function for Case 10b, characterized by relatively short incident waves ($k_p^{(1)}d = 1.7$) with a fairly narrow-band spectrum ($\gamma = 20$), is shown in Fig. 9. The theoretical distribution in that figure is a two-term Gram–Charlier expansion (Longuet-Higgins, 1963), which can be expressed as

$$p\left(\zeta'\right) = \frac{P\left(\zeta', \mathrm{Sk}\right)}{\sqrt{2\pi}} \exp\left[-\frac{1}{2}\left(\zeta'\right)^2\right]. \tag{14}$$

For $P = 1$ this is the normalized Gaussian distribution, whereas for the nonlinear pdf the polynomial $P(\zeta',\mathrm{Sk})$ depends only on variance and skewness (for details of P, see Longuet-Higgins, 1963).

At the edge of the surf zone (left panel of Fig. 9) the pdf is strongly skewed, which increases at the locations further inside the surf zone (center and right panel of Fig. 9). The deviation from the Gaussian distribution shows that the waves are nonlinear, with relatively sharp and tall peaks, and shallow and elongated troughs, which shows that a nonlinear wave model is required to reliably estimate surf zone statistics. Although a direct comparison with the observed pdf for $|\zeta'| > 3$ is difficult due to the relatively short time series (and thus relatively low data density to populate the tails of the distribution), the agreement between the observations, Monte Carlo simulations, and the theoretical distribution is very good. Comparisons for other cases showed similar agreement (not shown). This shows that nonlinear effects are important for surf zone statistics, but that knowledge of the lowest two moments, variance and skewness, suffices to capture the principal characteristic of the pdf. As shown in the model results, SWASH can accurately model and predict these moments.

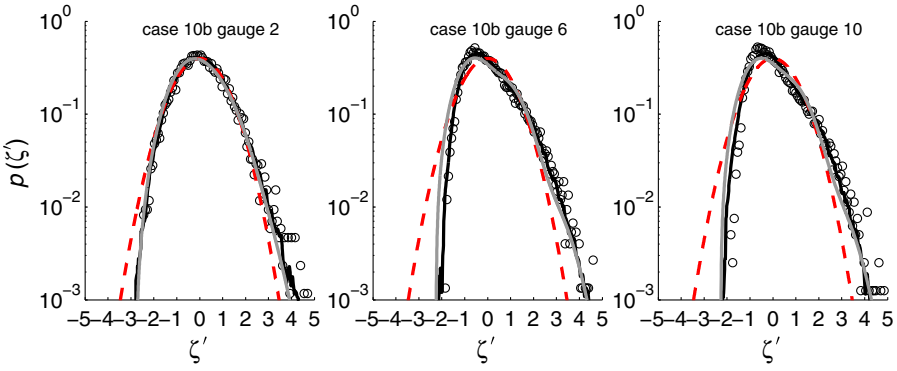

Fig. 9. Probability density functions (pdf) for the normalized free surface $\zeta' = \zeta/\sqrt{m_0}$ estimated from the observations (circles) and from the Monte Carlo simulations (solid black line), compared with a Gaussian distribution (dashed red line) and a two-term Gram–Charlier (Eq. (14)) series (gray line) using the skewness values obtained from the Monte Carlo simulations.

5.2. Spectral distribution of dissipation

Energy dissipation due to wave breaking is arguably the most important, and yet the least understood process in the surf zone (e.g. Peregrine, 1983). In general, bulk dissipation rates are reasonably well estimated by semi-empirical formulations based on a bore analogy (e.g. see Salmon and Holthuijsen, in preparation, for an extensive overview), however, spectral models require a spectral distribution of the dissipation, which is not available from theory or observations. As a consequence, spectral breaker dissipation functions $D(f)$ are invariably expressed as $D(f) = D_0 D'(f)$, where $D'(f)$ is an unknown distribution function, for which $\int D'(f)df = 1$ and D_0 is the bulk dissipation. Eldeberky and Battjes (1996) assumed that the distribution function $D'(f)$ is proportional to the normalized spectrum, $D'(f) = E'(f) = E(f)/m_0$, where $E'(f) = E(f)/m_0$, so that dissipation is stronger in the more energetic ranges of the spectrum. Other studies found that better results for third-order bulk statistics are obtained by weighting the dissipation function toward higher frequencies using $D'(f) = f^2 E'(f)$ (e.g. Chen et al., 1997; Kirby and Kaihatu, 1996), or a linear combination of the two shapes (Mase and Kirby, 1992). Weighting the dissipation toward higher frequencies is consistent with the observation that dissipation takes place mostly at the higher frequencies but is not very strong in the energy-carrying ranges (see e.g. Section 4.4 of the present work or e.g. Herbers et al., 2000).

In SWASH, we do not impose any distribution as wave breaking is handled in the time domain, but the resulting spectral signature can be estimated from the model results. Assuming that dissipation is the term responsible for closing the balance between F_x and S_{nl}, i.e. $D(f,x) = F_x(f,x) - S_{nl}(f,x)$, $D'(f)$ can be directly estimated from the Monte Carlo simulation. In Fig. 10, we show the mean and standard deviation from the 31 Monte Carlo simulations for the ratio $D'(f)/E'(f)$, which measures the dissipation rate at each frequency relative to the amount of energy. In the presence of strong dissipation in the inner surf zone, the mean of D'/E' strongly emphasizes higher frequencies (see Fig. 10). At deeper, more offshore, locations (i.e. gauge 2–5) dissipation is weak, so that $D'(f)/E'(f)$ is more variable and noisy, and no clear pattern can be discerned (not shown). For $f < 2$ Hz the computed ratio can become slightly negative, which would seem to imply 'positive dissipation', but is likely caused by small relative errors in the estimation of S_{nl} and F, which dominate the balance in this region (although dissipation is small here, it results as the difference of two large, but opposing, terms). Overall, the model-predicted dissipation rate $D'(f)$ agrees fairly well with the earlier suggested f^2 weighting (see Fig. 10). Since in SWASH $D'(f)$ is not prescribed but rather follows from the Monte Carlo data directly, this result appears to corroborate the use of an f^2 weighting for breaking dissipation. More generally, this also illustrates how a fairly detailed non-hydrostatic model can be a valuable tool in developing or testing parameterizations uses in operational (e.g. Booij et al., 1999; Tolman, 1991) or research spectral wave models.

6. Conclusions

In the present work we considered modeling of wave dynamics in the surf zone using the non-hydrostatic model SWASH. Detailed comparison to flume observations shows that a relatively efficient model such as SWASH, in which the details of the breaking process such as overturning and turbulence are not resolved, can reliably predict surf zone (non-Gaussian) wave statistics. Our results show that even without calibration or fine-tuning, the model accurately predicts both second-order bulk parameters such as wave height and period, higher-order statistics, including skewness and asymmetry of the waves, and the details of the spectral evolution (up to 10 times the peak frequency). The generally excellent agreement between the model results and the observations, demonstrates that the model accurately captures the macro-effects of the dominant nonlinear and dissipative processes in the surf zone, in particular the triad wave–wave interactions and the dissipation due to breaking. These results show that for the predominantly spilling breaker conditions considered, a non-hydrostatic model with a single-valued representation of the free surface, can provide an accurate presentation of the wave statistics in the surf zone. Hence, the representation of the free-surface as a single-valued function appears not to prevent an accurate representation of the wave statistics in the surf zone, at least in case of spilling breakers. The pdf of the free-surface, estimated by Monte Carlo simulations, compares well with a theoretical nonlinear pdf that depends on the first two moments, variance and skewness, both of which can be reliably estimated from SWASH simulations. From the energy balance we derived that the wave dissipation in SWASH is proportional to a frequency-squared distribution function, which is consistent with observations in other studies. Although the present study considers one-dimensional wave propagation in a flume, we note that triad nonlinear and dissipation processes are not fundamentally different for 2D surf zones with short-crested waves, so that our conclusions are probably also valid under such conditions. Overall, the findings of this study suggest that SWASH is a viable tool for modeling wave and wave-driven dynamics in a nonlinear, dissipative surf zone.

Acknowledgments

This research is supported by the U.S. Office of Naval Research (Littoral Geosciences and Optics Program and Physical Oceanography Program) and by the National Oceanographic Partnership Program.

Appendix A. Frequency dispersion in SWASH

To a large extent, the magnitude of the nonlinear transfers is determined by the resonant mismatch, $\Delta\omega(k_1,k_2) = \omega(k_1) + \omega(k_2) - \omega(k_1 + k_2)$ among a triad of waves with wavenumber k_1, k_2, k_3 so that $k_3 = k_1 + k_2$. A correct representation of nonlinear interactions therefore not only requires a good approximation to linear dispersion

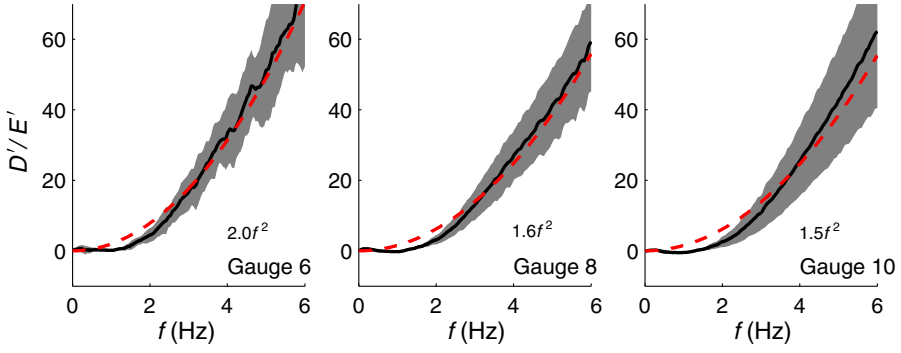

Fig. 10. Mean (over all 31 cases) of the distribution function scaled with the normalized energy, $D'(f)/E'$ (solid black line), compared with a least squares fit αf^2 shape. The patched area indicates the region within one standard deviation of the mean.

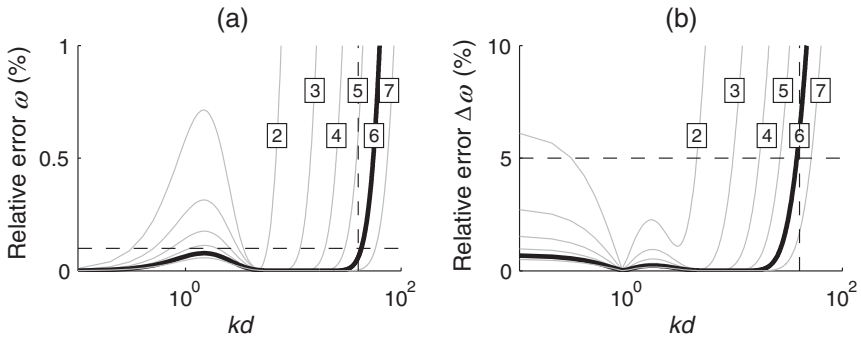

Fig. A.1. Absolute relative error (in percent) in (a) the angular frequency $\omega(k)$, and (b) resonant mismatch for self–self interactions $\Delta\omega(k,k) = 2\omega(k) - \omega(2k)$, when using the dispersion relation obtained from an N layer system, ω_N compared to using the linear dispersion relation, ω, as a function of the relative depth kd. Depicted are the error curves for N between 2 to 7, which shows that for $N = 6$ (thick solid line) the error remains below 0.1 and 5% (horizontal dashed lines), respectively, for $kd < 40$ (vertical dashed line).

of the three interacting components, but also of their resonant mismatch. In general, for non-hydrostatic models, the horizontal scales are well resolved, whereas the vertical resolution is relatively coarse. Hence the accuracy of the linear dispersive behavior of the numerical model is largely determined by the vertical resolution, and can therefore be estimated from the semi-discrete system obtained by discretization of the vertical. In the case of SWASH, the linear, semi-discrete system corresponding to Eqs. (1) to (4), for N vertical layers, is given by application of an edge-based grid in the vertical combined with the Keller-box approximation for the vertical pressure gradients,

$$\frac{\partial u_{n-\frac{1}{2}}}{\partial t} + g\frac{\partial \zeta}{\partial x} + \frac{1}{2}\frac{\partial p_n^{\mathrm{nh}}}{\partial x} + \frac{1}{2}\frac{\partial p_{n-1}^{\mathrm{nh}}}{\partial x} = 0, \qquad n = 1\,..N, \tag{A.1}$$

$$\frac{\partial w_n}{\partial t} + \frac{\partial w_{n-1}}{\partial t} + 2\frac{p_n^{\mathrm{nh}} - p_{n-1}^{\mathrm{nh}}}{\Delta z} = 0, \qquad n = 1\,..N, \tag{A.2}$$

$$\frac{\partial u_{n-\frac{1}{2}}}{\partial x} + \frac{w_n - w_{n-1}}{\Delta z} = 0, \qquad n = 1\,..N, \tag{A.3}$$

$$\frac{\partial \zeta}{\partial t} + \Delta z \sum_{n=1}^{N} \frac{\partial u_{n-\frac{1}{2}}}{\partial x} = 0. \tag{A.4}$$

Here, the nth pressure and vertical velocity components, p_n and w_n (with $n \in \{0 \ldots N\}$) are located on the layer interface, whereas the layer averaged velocity $u_{n-\frac{1}{2}}$ (with $n \in \{1 \ldots N\}$) are located in the central plane, where $\{\ldots\}_n = \{\ldots\}(x,z_n,t)$ with $z_n = n\Delta z$ - d, with $\Delta z = d/N$. From the dynamic boundary condition at the free surface we have $p_N^{\mathrm{nh}} = 0$. Moreover, if we assume a horizontal bottom, we obtain from the kinematic boundary condition at the bed that $w_0 = 0$. If we then consider the initial value problem on an infinite domain, we can associate $\partial_t\zeta \rightarrow -i\omega\hat{\zeta}(k,\omega)$, and $\partial_x \rightarrow ik\hat{\zeta}(k,w)$, and similarly for $u_{n-\frac{1}{2}}, w_n$, to obtain for each mode ω, k a $(3N + 1) \times (3N + 1)$ linear system $A(k,\omega)$ in terms of the Fourier amplitudes

$$\hat{y} = \left[\hat{u}_{\frac{1}{2}}, \ldots, \hat{u}_{N-\frac{1}{2}}, \hat{w}_1, \ldots, \hat{w}_N, \hat{p}_0, \ldots, \hat{p}_{N-1}, \hat{\zeta}\right], \tag{19}$$

so that $A\hat{y} = 0$. For this system to have solutions other than the trivial solution, A must be singular, or $\mathrm{Det(A)} = 0$, resulting in a polynomial relating ω and k, from which the linear dispersion relation $\omega_N(k)$ that corresponds to the N layer system can be determined. As the calculations quickly become involved for $N > 1$, this is done using a symbolic algebra system.[2]

From ω_N thus obtained, it can be seen that, assuming the horizontal scales are well resolved, the number of layers required to accurately model dispersion mainly depends on the maximum relative depth within the frequency range of interest (see Fig. A.1a). In the present work this corresponds to waves with $f < 4$ Hz, or $kd < 40$. By using 6 layers, the maximum relative error for $kd < 40$ remains below 0.1%. A similar analysis can be made for the frequency mismatch $\Delta\omega(k_1, k_2)$, when considering the mismatch for the self–self interactions, $\Delta\omega(k, k)$, for different values of kd (see Fig. A.1b). This shows that for 6 layers, the relative error is less than 6% for $kd < 40$.

[2] Implemented by using the Matlab Symbolic Toolbox.

References

Battjes, J.A., Bakkenes, H.J., Janssen, T.T., van Dongeren, A.R., 2004. Shoaling of subharmonic gravity waves. J. Geophys. Res. Oceans 1090 (C2), C02009.

Becq-Girard, F., Forget, P., Benoit, M., 1999. Non-linear propagation of unidirectional wave fields over varying topography. Coast. Eng. 380 (2), 91–113.

Booij, N., Ris, R.C., Holthuijsen, L.H., 1999. A third-generation wave model for coastal regions 1. Model description and validation. J. Geophys. Res. Oceans 104, 7649–7666.

Bouws, E., Gunther, H., Rosenthal, W., Vincent, C.L., 1985. Similarity of the wind wave spectrum in finite depth water 1. Spectral form. J. Geophys. Res. Oceans 900 (C1), 975–986.

Chen, Y., Guza, R.T., Elgar, S., 1997. Modeling spectra of breaking surface waves in shallow water. J. Geophys. Res. Oceans 1020 (C11), 25035–25046.

Chow, V. Te, 1959. Open-Channel Hydraulics. McGraw-Hill.

Eldeberky, Y., Battjes, J.A., 1996. Spectral modeling of wave breaking: application to Boussinesq equations. J. Geophys. Res. Oceans 1010 (C1), 1253–1264.

Elgar, S., Guza, R.T., 1985. Observations of bispectra of shoaling waves. J. Fluid Mech. 161, 425–448.

Herbers, T.H.C., Burton, M.C., 1997. Nonlinear shoaling of directionally spread waves on a beach. J. Geophys. Res. Oceans 102, 21101–21114.

Herbers, T.H.C., Russnogle, N.R., Elgar, S., 2000. Spectral energy balance of breaking waves within the surf zone. J. Phys. Oceanogr. 300 (11), 2723–2737.

Herbers, T.H.C., Orzech, Mark, Elgar, Steve, Guza, R.T., 2003. Shoaling transformation of wave frequency-directional spectra. J. Geophys. Res. Oceans 1080 (C1), 3013.

Hoefel, F., Elgar, S., 2003. Wave-induced sediment transport and sandbar migration. Science 299, 1885–1887.

Holthuijsen, L.H., 2007. Waves in Oceanic and Coastal Waters. Cambridge Univ. Press.

Janssen, T.T., 2006. Nonlinear Surface Waves over Topography. Ph.D. dissertation University of Technology, Delft.

Janssen, T.T., Battjes, J.A., van Dongeren, A.R., 2003. Long waves induced by short-wave groups over a sloping bottom. J. Geophys. Res. Oceans 1080 (C8).

Kaihatu, J.M., Veeramony, J., Edwards, K.L., Kirby, J.T., 2007. Asymptotic behavior of frequency and wave number spectra of nearshore shoaling and breaking waves. J. Geophys. Res. Oceans 1120 (C6).

Kirby, J.T., Kaihatu, J.M., 1996. Structure of frequency domain models for random wave breaking. Proc. 25th Int. Conf. Coastal Eng. ASCE, pp. 1144–1155.

Komen, G.J., Cavaleri, L., Donelan, M., Hasselmann, K., Hasselmann, S., Janssen, P.A.E.M., 1994. Dynamics and Modelling of Ocean Waves. Cambridge Univ. Press.

Lam, D.C.L., Simpson, R.B., 1976. Centered differencing and the box scheme for diffusion convection problems. J. Comput. Phys. 220 (4), 486–500.

Launder, B.E., Spalding, D.B., 1974. The numerical computation of turbulent flows. Comput. Methods Appl. Mech. Eng. 30 (2), 269–289.

Longuet-Higgins, M.S., 1963. The effect of non-linearities on statistical distributions in the theory of sea waves. J. Fluid Mech. 17, 459–480.

Longuet-Higgins, M.S., 1970. Longshore currents generated by obliquely incident sea waves, 1. J. Geophys. Res. Oceans 750 (33), 6778–6789.

Longuet-Higgins, M.S., Stewart, R.W., 1964. Radiation stresses in water waves; a physical discussion, with applications. Deep Sea Res. 110 (4), 529–562.

Ma, G., Shi, F., Kirby, J.T., 2012. Shock-capturing non-hydrostatic model for fully dispersive surface wave processes. Ocean Model. 43–440, 22–35.

MacMahan, J.H., Thornton, E.B., Reniers, A.J.H.M., 2006. Rip current review. Coast. Eng. 530 (2–3), 191–208.

Madsen, P.A., Svendsen, I.A., 1983. Turbulent bores and hydraulic jumps. J. Fluid Mech. 129, 1–25.
Madsen, P.A., Bingham, H.B., Liu, H., 2002. A new Boussinesq method for fully nonlinear waves from shallow to deep water. J. Fluid Mech. 462, 1–30.
Mase, H., Kirby, J.T., 1992. Hybrid frequency-domain KdV equation for random wave transformation. Proc. 28th Int. Conf. Coastal Eng., Venice. ASCE, pp. 474–487.
Nwogu, O., 1993. Alternative form of Boussinesq equations for nearshore wave propagation. J. Waterw. Port Coast. Ocean Eng. 1190 (6), 618–638.
Peregrine, D.H., 1967. Long waves on a beach. J. Fluid Mech. 270 (4), 815–827.
Peregrine, D.H., 1983. Breaking waves on beaches. Annu. Rev. Fluid Mech. 15, 149–178.
Salmon, J.E., Holthuijsen, L.H., 2013n. Depth-induced wave breaking for third-generation wave models 1. Review and verification (Manuscript in preparation).
Smit, P.B., Janssen, T.T., 2013. The evolution of inhomogeneous wave statistics through a variable medium. J. Phys. Oceanogr. 43, 1741–1758.
Smit, P.B., Zijlema, M., Stelling, G.S., 2013. Depth-induced breaking in a non-hydrostatic nearshore wave model. Coast. Eng. 76, 1–16.
Smith, J.M., 2004. Shallow-water spectral shapes. Proc. 29th Int. Conf. Coastal Eng. World Scientific, pp. 206–217.
Smith, J.M., Vincent, C., 1992. Shoaling and decay of two wave trains on beach. J. Waterw. Port Coast. Ocean Eng. 1180 (5), 517–533.
Smith, J.M., Vincent, L., 2003. Equilibrium ranges in surf zone wave spectra. J. Geophys. Res. Oceans 1080 (C11).
Stelling, G.S., Duinmeijer, S.P.A., 2003. A staggered conservative scheme for every Froude number in rapidly varied shallow water flows. Int. J. Numer. Methods Fluids 430 (12), 1329–1354.
Stelling, G.S., Zijlema, M., 2003. An accurate and efficient finite-difference algorithm for non-hydrostatic free-surface flow with application to wave propagation. Int. J. Numer. Methods Fluids 430 (1), 1–23.
Svendsen, I.A., 1984. Mass flux and undertow in a surf zone. Coast. Eng. 80 (4), 347–365.
The WAMDI Group, 1988. The WAM model — a third generation ocean wave prediction model. J. Phys. Oceanogr. 180 (12), 1775–1810.
Ting, F.C.K., Kirby, J.T., 1994. Observation of undertow and turbulence in a laboratory surf zone. Coast. Eng. 240 (1–2), 51–80.
Tissier, M., Bonneton, P., Marche, F., Chazel, F., Lannes, D., 2012. A new approach to handle wave breaking in fully non-linear Boussinesq models. Coast. Eng. 670, 54–66.
Tolman, H.L., 1991. A third-generation model for wind waves on slowly varying, unsteady, and inhomogeneous depths and currents. J. Phys. Oceanogr. 210 (6), 782–797.
Tonelli, M., Petti, M., 2012. Shock-capturing Boussinesq model for irregular wave propagation. Coast. Eng. 610, 8–19.
Torres-Freyermuth, A., Losada, I.J., Lara, J.L., 2007. Modeling of surf zone processes on a natural beach using Reynolds-averaged Navier–Stokes equations. J. Geophys. Res. Oceans 1120 (C9).
van Dongeren, A.R., Battjes, J.A., Janssen, T.T., van Noorloos, J., Steenhauer, K., Steenbergen, G., Reniers, A., 2007. Shoaling and shoreline dissipation of low-frequency waves. J. Geophys. Res. Oceans 1120 (C2).
Wei, G., Kirby, J.T., Grilli, S.T., Subramanya, R., 1995. A fully non-linear Boussinesq model for surface waves. Part 1. Highly non-linear unsteady waves. J. Fluid Mech. 294, 71–92.
Wise Group, 2007. Wave modelling — the state of the art. Prog. Oceanogr. 750 (4), 603–674.
Yamazaki, Y., Kowalik, Z., Cheung, K.F., 2009. Depth-integrated, non-hydrostatic model for wave breaking and run-up. Int. J. Numer. Methods Fluids 610 (5), 473–497.
Zakharov, V., 1999. Statistical theory of gravity and capillary waves on the surface of a finite-depth fluid. Eur. J. Mech. Fluids 180 (3), 327–344.
Zijlema, M., Stelling, G.S., Smit, P.B., 2011. SWASH: an operational public domain code for simulating wave fields and rapidly varied flows in coastal waters. Coast. Eng. 580 (10), 992–1012.